In-situ Investigation of Expansion during Lithiation of Pillared MXene with Ultralarge Interlayer Distance

Philip A. Maughan,[1] Stefanie Arnold,[2,3] Yuan Zhang,[2,3] Volker Presser,[2,3] Nuria Tapia-Ruiz,[4] and Nuno Bimbo[1¥*]

[1] Department of Engineering, Lancaster University, Lancaster, LA1 4YW, United Kingdom
[2] INM - Leibniz Institute for New Materials, Saarbrücken, 66123, Germany
[3] Department of Materials Science and Engineering, Saarland University, 66123 Saarbrücken, Germany
[4] Department of Chemistry, Lancaster University, Lancaster, LA1 4YB, United Kingdom
[¥] Current address: School of Chemistry, Highfield Campus, University of Southampton, Southampton, SO17 1BJ, United Kingdom
[*] Corresponding author's email: N.Bimbo@soton.ac.uk

Abstract

Pillared $Ti_3C_2T_z$ MXene with large interlayer spacing (1.75 nm) is shown to be promising for high-power Li-ion batteries. Pillaring dramatically enhances the electrochemical performance, with superior capacities, rate capability and cycling stability compared to the non-pillared material. In particular, at a high rate of 1 A g^{-1}, the SiO_2-pillared MXene has a capacity over 4.2 times that of the non-pillared material. For the first time, we apply in-situ electrochemical dilatometry to study the volume changes within the MXenes during (de)lithiation. The pillared MXene has superior performance despite larger volume changes compared to the non-pillared material. These results give key fundamental insights on the behaviour of $Ti_3C_2T_z$ electrodes in organic Li electrolytes and demonstrate that MXene electrodes should be designed to maximise interlayer spacings, and that MXenes can tolerate significant initial expansions. After 10 cycles, both MXenes show nearly reversible thickness changes after the charge-discharge process, explaining the stable long-term electrochemical performance.

Main Text

MXenes are a family of two-dimensional materials first reported in 2011, which have shown promising performance in electrochemical energy storage applications such as metal-ion batteries and supercapacitors.[1–3] However, their electrochemical performance is highly dependent on the electrode architecture, with multilayered stacked MXene suffering from

low capacities and poor rate capabilities and cycling stabilities.[4,5] This has increased focus on developing porous MXenes with controlled and open architectures to enhance electrochemical performance, such as flocculation, freeze drying and pillaring.[6–8]

Pillaring introduces foreign species between the layers to act as pillars, allowing pore sizes to be tuned by pillar choice and heat treatment steps.[9] Recently, these techniques have been adapted to create porous MXenes for electrochemical applications, including metal-ion batteries, hybrid metal-ion capacitors, and supercapacitors.[10–18] For example, pillar species such as hexadecyl trimethylammonium bromide (CTAB), SnS and Sn cations have been utilised to enlarge the interlayer spacing and improve the performance of MXene electrodes in Li-ion batteries.[10,16–18] However, while it is well established that pillaring can significantly enhance electrochemical performance, an in-depth understanding of the processes occurring in pillared structures during cycling is lacking.

In this work, we utilise in-situ electrochemical dilatometry (eD) supported by X-ray diffraction (XRD) to rationalize the enhanced performance of silica-pillared $Ti_3C_2T_z$ MXene as a negative electrode for Li-ion batteries. In-situ eD has previously been applied to MXene research to study the intercalation of various ions and molecules in several electrolyte systems such as ionic liquids[19,20] and aqueous Li, Na and Mg systems.[21–23] However, this is the first time this technique has been applied to MXenes for organic Li-ion battery systems, and can provide important information about the effect of pillars during (de)lithiation.

The pillared $Ti_3C_2T_z$ MXene (Ti_3C_2-Si-400) was synthesized by our previously reported pillaring method using tetraethylortho silicate (TEOS) as the silica source and dodecylamine (DDA) as the co-pillar amine (**Figure 1a**).[24] Full details of all synthesis and characterization methods can be found in the experimental section in Supporting Information. The successful intercalation and pillaring of the synthesized $Ti_3C_2T_z$ MXene were confirmed by PXRD data (**Figure 1b,** *Supporting Information* **Figure S1a**), while scanning electron microscopy (SEM) confirmed the retention of the layered morphology, (**Figure 1c,** *Supporting Information* **Figure S1b**), which matches our previous report.[24] We note that our pillared structure is based on multilayered MXenes, and delamination was not attempted since delamination procedures can suffer from issues, such as low yield (52-60%), multiple steps, and low concentrations of delaminated nanosheets in solution.[25] One of the potential attractions of pillaring techniques is to allow

full access of the MXene nanosheet layers in a stable electrode architecture using simple methods.

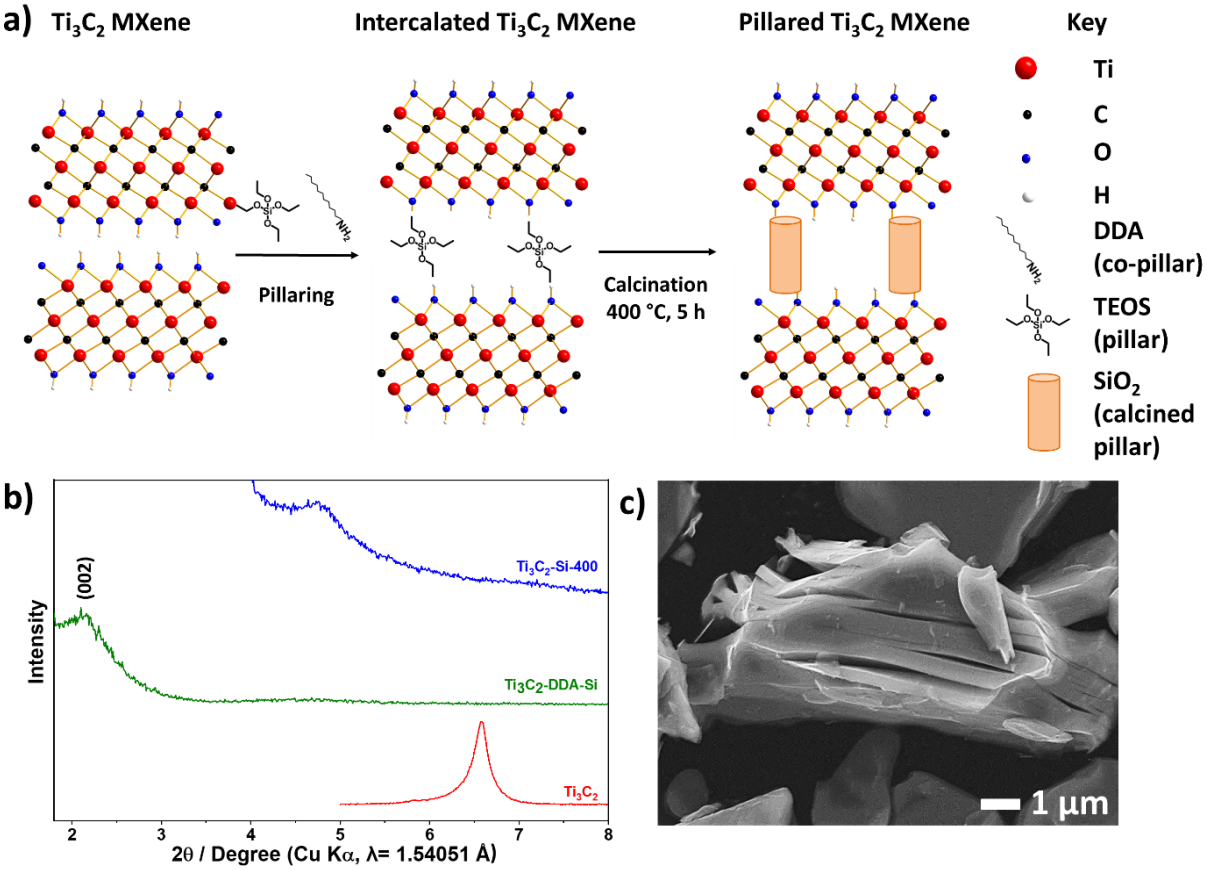

Figure 1. a) Schematic illustration of the amine-assisted SiO_2 pillaring process used to create porous $Ti_3C_2T_z$ with enlarged interlayer distance. **b)** Low angle (1.8-8° 2θ) PXRD data demonstrating expanded interlayer spacing in the SiO_2-pillared MXene (Ti_3C_2-Si-400), intercalated MXene (Ti_3C_2-DDA-Si) and non-pillared MXene (Ti_3C_2). **c)** SEM micrograph of the SiO_2-pillared MXene (Ti_3C_2-Si-400).

Galvanostatic charge-discharge (GCD) experiments were used to investigate the performance of the pillared $Ti_3C_2T_z$ as a Li-ion battery electrode (**Figure 2**), with a specific current of 20 mA g^{-1} and a potential window of 0.01-3.0 V vs. Li^+/Li. All further potentials in the manuscript are referenced vs. Li^+/Li. The voltage profiles of the pillared and non-pillared MXenes display similar features, with a linear region between 3.0-0.3 V followed by a short plateau feature below 0.3 V. This signifies that Li storage in $Ti_3C_2T_z$ is a two-stage process, as previously reported.[26] The first stage corresponds to Li^+ intercalation between $Ti_3C_2T_z$ nanosheets forming $Li_2Ti_3C_2T_z$ (theoretical capacity of 260 mAh g^{-1}), followed by Li^+ adsorption

above the first intercalated layer, resulting in $Li_3Ti_3C_2T_z$, in the lower voltage region. An additional short plateau is observed on the initial discharge for both materials, which is commonly assigned to solid electrolyte interphase (SEI) formation, and irreversible reactions between Li and MXene surface groups.[26–28] Both materials also show typical linear charge profiles, with a small plateau around 1.5 V, resulting from Li de-intercalation.

The pillared MXene has a significantly larger first discharge capacity (536 mAh g^{-1}) compared with the non-pillared (289 mAh g^{-1}), and a larger initial Coulombic efficiency (58% and 43%, respectively). The enhanced initial Coulombic efficiency can be explained by lower levels of Li trapping due to the enlarged interlayer spacings which would provide open Li diffusion channels. Also, surface groups such as -OH, which have been reported to react irreversibly during lithiation, are likely to have already reacted with the co-pillars during the pillaring process. This would further reduce irreversible capacity losses during (de)lithiation.[26] For the second discharge cycle, the pillared $Ti_3C_2T_z$ shows capacities around 2.2 times greater than the non-pillared material (314 mAh g^{-1} and 142 mAh g^{-1}, respectively), likely as a result of the larger interlayer spacing facilitating greater ion accessibility to the MXene redox sites.

Significantly, the 2nd discharge capacity (314 mAh g^{-1}) is considerably higher than expected based on monolayer lithium coverage, which is 235 mAh g^{-1} when accounting for the pillar mass (which is estimated to be 11 wt. % based on SEM-EDS analysis, *Supporting Information,* **Figure S2**), further implying that multilayer adsorption is contributing to the capacity. However, the full formation of a third lithium layer to form $Ti_3C_2O_2Li_3$ would give a capacity of around 350 mAh g^{-1}, which suggests that the third layer does not fully form. Xie et al. calculated that the extra adsorbed Li layer would be located around 2.8 Å above the Ti-O-Li lithium,[26] which requires an interlayer gallery space of at least 6 Å. This is less than the ca. 7 Å interlayer gallery space calculated from XRD data in our pillared MXene, demonstrating the feasibility of this charge storage mechanism, illustrated by the insets in **Figure 2a**-**b**. Note that the interlayer gallery space is defined as the free pore space between layers of a pillared material, and is not equivalent to the *d*-spacing, which includes the sheet thickness. Our pillared $Ti_3C_2T_z$ has a *d*-spacing of 1.75 nm, as calculated from the (*002*) peak using the Bragg equation. An extra increase of 2.3 Å gallery space would be required for the adsorption of a further layer,[26] taking the total to at least 8.3 Å, which is larger than our spacings, revealing why further adsorption does not occur. Although the average interlayer gallery space was

calculated to be 0.7 nm from XRD data using a monolayer $Ti_3C_2T_z$ thickness of just under 1 nm, in line with the method utilized by Luo et al,[10] our previous work using transmission electron microscopy (TEM) revealed local variations in the gallery spacings across the pillared material,[24] with some areas having spacings less than 0.7 nm, explaining why a full extra adsorption layer was not formed.

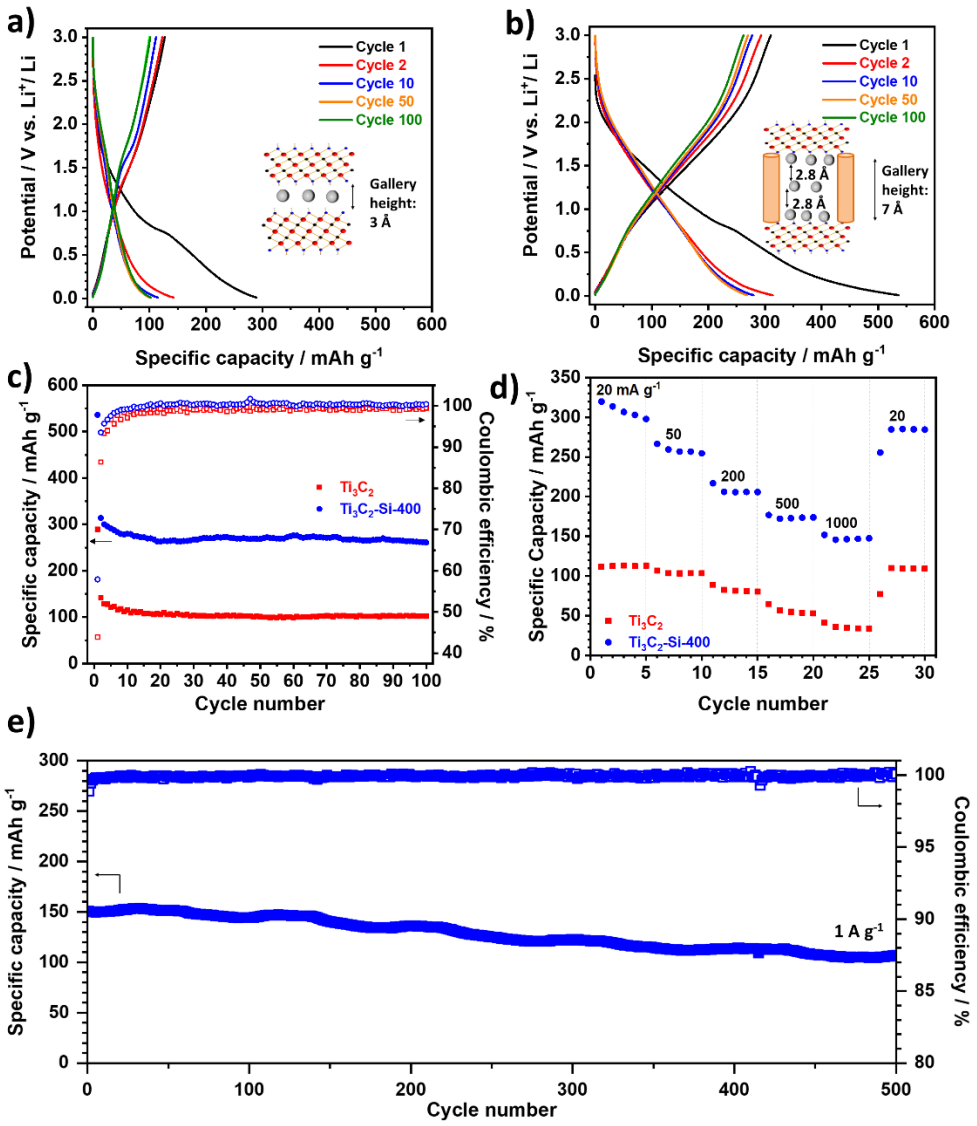

Figure 2. Galvanostatic data from half-cell tests against Li metal at 20 mA g^{-1} in the voltage range 0.01-3.0 V using 1 M $LiPF_6$ in EC:DEC (1:1 mass ratio) as the electrolyte. Load curves for selected cycles for **a)** non-pillared $Ti_3C_2T_z$ and **b)** SiO_2-pillared $Ti_3C_2T_z$ (Ti_3C_2-Si-400). **Insets** illustrate the lithium layers (grey circles) in the respective MXene (blue rectangles) after lithiation (0.01 V). **c)** Coulombic efficiency and discharge capacities of the pillared and non-pillared samples over 100 cycles. **d)** Rate capability tests for the pillared and non-pillared

MXene at rates of 20, 50, 200, 500 and 1000 mA g^{-1}. Five cycles are shown for each rate. **e)** Galvanostatic charge-discharge data for SiO_2-pillared $Ti_3C_2T_z$ in a Li-ion half-cell tested for 500 cycles at a rate of 1 A g^{-1} in a potential window of 0.01-3.0 V.

The pillared MXene also showed improved capacity retention (83%, 262 mAh g^{-1}) compared with the non-pillared MXene (72%, 101 mAh g^{-1}) over 100 cycles (**Figure 2c)**. The majority of the capacity fade occurred over the initial 15 cycles, with capacity retentions of 96% (pillared) and 91% (non-pillared) between cycles 15 to 100. These results demonstrate that the SiO_2 pillars significantly improve electrode stability during cycling.

The rate capability of the MXenes was investigated by cycling at rates of 20, 50, 200, 500, 1000 and 20 mA g^{-1}, with five cycles conducted at each rate (**Figure 2d**). The pillared MXene out-performed the non-pillared material at all rates tested, with discharge capacities of 307, 260, 206, 173, 147 and 285 mAh g^{-1} at the respective rate compared to 113, 104, 82, 55, 35 and 109 mAh g^{-1}, respectively. Interestingly, the capacity enhancement is more considerable at higher rates than lower ones, with an increase of 4.2 times that of the non-pillared $Ti_3C_2T_z$ observed at 1 A g^{-1}, compared with just 2.7 times at 20 mA g^{-1}. This demonstrates that the pillared architecture benefits the high rate performance in particular, and implies that the enlarged interlayer distance increases the lithium storage capacity and creates channels that allow fast Li^+ ion diffusion through the structure. Cycling the pillared MXene at 1 A g^{-1} for a further 500 cycles after the rate capability tests resulted in a discharge capacity of 151 mAh g^{-1} (**Figure 2e**) with a capacity retention of 71%, which shows reasonable stability at high rates. The impressive high rate performance can be explained by the significant contribution of a surface-limited capacitive-like process to the charge storage, revealed by *b*-value analysis conducted on cyclic voltammetry (CV) data collected at multiple scan rates (*Supporting Information,* **Figure S4 a-b**). At potentials above 0.5 V, the *b*-values are at least 0.85, consistent with mostly capacitive charge storage behavior. An ideal capacitor would display a *b*-value of 1, whereas an ideal diffusion-limited battery-like electrode would have $b = 0.5$.[29] Furthermore, deconvolution of the capacitive and diffusion-limited charge storage processes, following the method described by Wang et al.,[30] revealed that at the scan rate of 5 mV s^{-1}, 78% of the total current was due to capacitive-like processes, demonstrating the importance of capacitive processes at high rates (*Supporting Information,* **Figure S4c**). A scan rate of 5 mV

s^{-1} corresponds to a sweep time of 10 min, similar to the sweep time of 8 min for the GCD testing at 1 A g^{-1}. Even at the low scan rate of 0.2 mV s^{-1}, 43% of the total charge storage was a result of capacitive-like processes (*Supporting Information*, **Figure S4d**). As observed in previous studies of MXenes in organic Li-ion systems, the capacitive contribution to the charge storage increased with increasing scan rate (*Supporting Information*, **Figure S4d**).[31,32] Further details on this analysis are given in the experimental section in the Supporting Information. This analysis uses a range of sweep rates, similar to other reported studies on pillared MXenes in organic electrolytes.[10,33]

To better understand the influence of interlayer gallery spacing on enhancing electrochemical lithium-ion storage, the volume change of pillared/non-pillared $Ti_3C_2T_z$ MXene during ion uptake and release was investigated by in-situ eD, which can observe volume change and CV simultaneously. A scan rate of 0.1 mV s^{-1} was applied with a narrower potential window of 0.01-2.5 V to focus on expansion/contraction processes related directly to (de)lithiation of the MXene. The CV shape for the pillared material closely matched with what was recorded in typical coin cells, with similar broad redox features, demonstrating that the cell used for in-situ eD[34] does not change the electrochemical processes. **Figure 3** shows the CV in the dilatometry cell and *Supporting Information,* **Figure S3** shows the comparison in a typical coin cell. The non-pillared material shows more pronounced redox-peaks compared with the pillared MXene, which are very broad, as was observed in our previous work in a Na-ion system and supports the expanded nature of the MXene.[24,35] As expected from the GCD data, multiple irreversible reduction peaks are observed in the pillared material during the first discharge, with peaks at around 1.3 V and 0.6 V attributed to the SEI formation and trapping of lithium-ions,[36] while lithiation of the conductive additive contributes to the peak at 0.01 V.[37,38] In the following delithiation sweep, two oxidation peaks were observed at 1.0 V and 1.8 V, representing the extraction of lithium ions, whose intensities continuously decrease slightly in the following cycles. For the non-pillared $Ti_3C_2T_z$ similar redox features occur, with pronounced reversible peaks at 1.8 V and 1.0 V (reduction) and at 0.9 V and 2.0 V (oxidation) throughout cycling. The fact that the CV and load curves for the non-pillared and pillared MXenes display similar features with no extra redox peaks/plateaus present in the data for the pillared MXene strongly implies that the enhanced performance results from the enlarged interlayer spacing, rather than electrochemical activity of the silica pillars. This is

consistent with the results of our previous work on pillared Mo_2TiC_2, where ex-situ x-ray photoelectron spectroscopy (XPS) and nuclear magnetic resonance spectroscopy (NMR) studies showed that the silica pillars in that system did not undergo lithiation during cycling.[15]

The unprocessed dilatometry data for the non-pillared MXene electrode reveals slight volume changes (~0.5 µm) during the initial 72 h of stabilization time, which is related to the electrode wetting process (**Figure 3c**). A relatively large expansion (1.84 µm, 5.7% strain) occurs during the first discharging step, consistent with Li^+ intercalation **(Figure 3a)**. At the end of the first lithiation sweep (0.01 V), a large jump is obervseed in the dilatometry data (**Figure 3a**). Comparison with the corresponding CV curve (**Figure 3a**) shows that while there is a large peak here, which likely results from a combination of Li intercalation, lithiation of the carbon additive,[38] and changes in MXene termination groups, the magnitude of this jump is significantly larger than corresponding CV peak. This implies that there is also significant contribution from device artifacts, which cannot be removed from the data in **Figure 3a** without losing physical meaning. However, it is clear that the contribution from artifacts is low overall and does not affect the conclusions that can be drawn from the data.

During de-lithiation, the expansion is only partially reversed, with a decrease in volume of ca. 1%. This demonstrates that $Ti_3C_2T_z$ remains in an expanded state even after de-lithiation, which is likely related to partial Li trapping, changes in MXene surface chemistry, SEI formation and solvent co-intercalation within the electrode layers. A similar pattern can be seen in the second cycle, but with reduced amplitude of volume changes on charge/discharge, while having a relative strain during the third cycle of -0.36%. Between cycles 3-10, the volume changes in the electrode appear to stabilize, with the magnitude of volume expansion on lithiation matching the magnitude of contraction on de-lithiation, so that the relative strain during the cycle tends towards zero. The pattern of expansion during lithiation and contraction during delithiation matches well with previous in-situ XRD studies carried out on multilayered Ti-based MXenes, which supports our dilatometry data.[39]

Since the volume changes in the stabilization time are artifacts of the device, a background/baseline subtraction was used in **Figure 3 c-d**. For the calculation of the relative and absolute expansion in **Table 1**, only the lithiation process was considered in each case. During the cycles, the non-pillared MXene behaves as a low strain material (<0.53% strain

within the entire lithiation cycle). The expansion levels for this sample increase slightly continuously up to the 10th cycle. Since the galvanostatic charge-discharge tests showed that the discharge capacity fades over these first 10 cycles, this may indicate the presence of irreversible side reactions, such as Li trapping. This would lead to a consistent expansion of the non-pillared material during cycling and explain the lower cycling stability for this material compared to the pillared MXene. The overall volume changes are very small for all cycles, which agrees well with the stable cycling performance observed during the GCD tests after the initial few cycles.

Post-mortem XRD recorded after 2 cycles of CV in custom-built polyether ether ketone (PEEK) cells of the non-pillared samples shows a slight shift in the (002) diffraction peak to lower angles (from 8.4° to 7.8° 2θ), supporting the small expansion observed in the dilatometry data (*Supporting Information,* **Figure S5 a-b)**).

For the pillared MXene (**Figure 3b and 3d**), a large initial expansion occurs over the first few hours under open circuit potential, with a gradual relaxation towards a minimum level of ca. 1.6 µm lower compared to the initial volume over the remainder of the rest period.

As observed for the non-pillared MXene, a large expansion (~1.02 µm) occurs in the first lithiation cycle (**Table 1**). The initial contraction has a smaller magnitude compared to the initial expansion. This suggests that the pillars aid in keeping the MXene electrode expanded, allowing wide Li-diffusion pathways rather than fixing a constant interlayer spacing. The pillared electrode continues to expand and contract over the next few cycles with approximately constant absolute and relative expansion. After the first cycle, the strain decreases slightly in the short term, but when looking at the continuous change, consistent values of around 3-4% relative strain can be obtained for all cycles. This correlates with the electrode's stable performance during galvanostatic charge/discharge cycling (**Figure 2d**). Simultaneously, slight capacity fading was observed over the first few cycles where the amplitude of contraction (de-lithiation) was consistently more minor than the previous expansion during lithiation, suggesting small quantities of irreversible side processes, such as Li trapping, were occurring, albeit significantly less than observed for the non-pillared material. Post-mortem XRD on the pillared MXene after two cycles shows a loss of the (002) diffraction peak (*Supporting Information,* **Figure S5d**), suggesting the expansions observed in

the dilatometry arise from inhomogeneous changes in the interlayer spacing during the initial (de)lithiation cycles. This early loss of observable diffraction peaks demonstrates the advantages of techniques such as in-situ dilatometry to study the (de)lithiation processes, which does not rely on long-range order.

Table 1. Comparison of the displacement and strain measured using in-situ electrochemical dilatometry for the non-pillared (Ti_3C_2) and pillared (Ti_3C_2-Si-400) MXenes. Background subtraction has been carried out to remove artifacts that are unrelated to the electrode shrinking and expansion and the data normalized by electrode thickness, according to the method reported by Budak et al.[40] These values were calculated by referring to the height change between the start of the cycle (2.5 V) and the opposite end of the lithiation process (0.01 V).

Cycle number	**Ti_3C_2**		**Ti_3C_2-Si-400**	
	Displacement (µm)	**Relative strain (%)**	**Displacement (µm)**	**Relative strain (%)**
Cycle 1	0.08	0.1	1.016	3.91
Cycle 3	0.15	0.35	0.693	2.69
Cycle 5	0.18	0.41	0.818	3.14
Cycle 10	0.23	0.53	0.799	3.07

The non-pillared MXene undergoes more minor volume changes than the pillared counterpart, which may be explained by the significantly larger quantities of Li intercalated into the structure (ca. 2.5 times) in the pillared electrode compared to the non-pillared. This implies that the key to unlocking high and persistent performance for MXenes is to engineer large interlayer spacings, which would avoid narrow interlayer spacings limiting Li storage capacity and diffusion. Large but reversible expansions do not seem to be detrimental to MXene performance. Pillared MXene undergoes large but consistent volume changes whilst displaying high cycling stability compared to the non-pillared MXene, where the expansion gradually increased in magnitude during cycling. This finding suggests that MXene architectures should be designed to minimise irreversible volume changes during cycling.

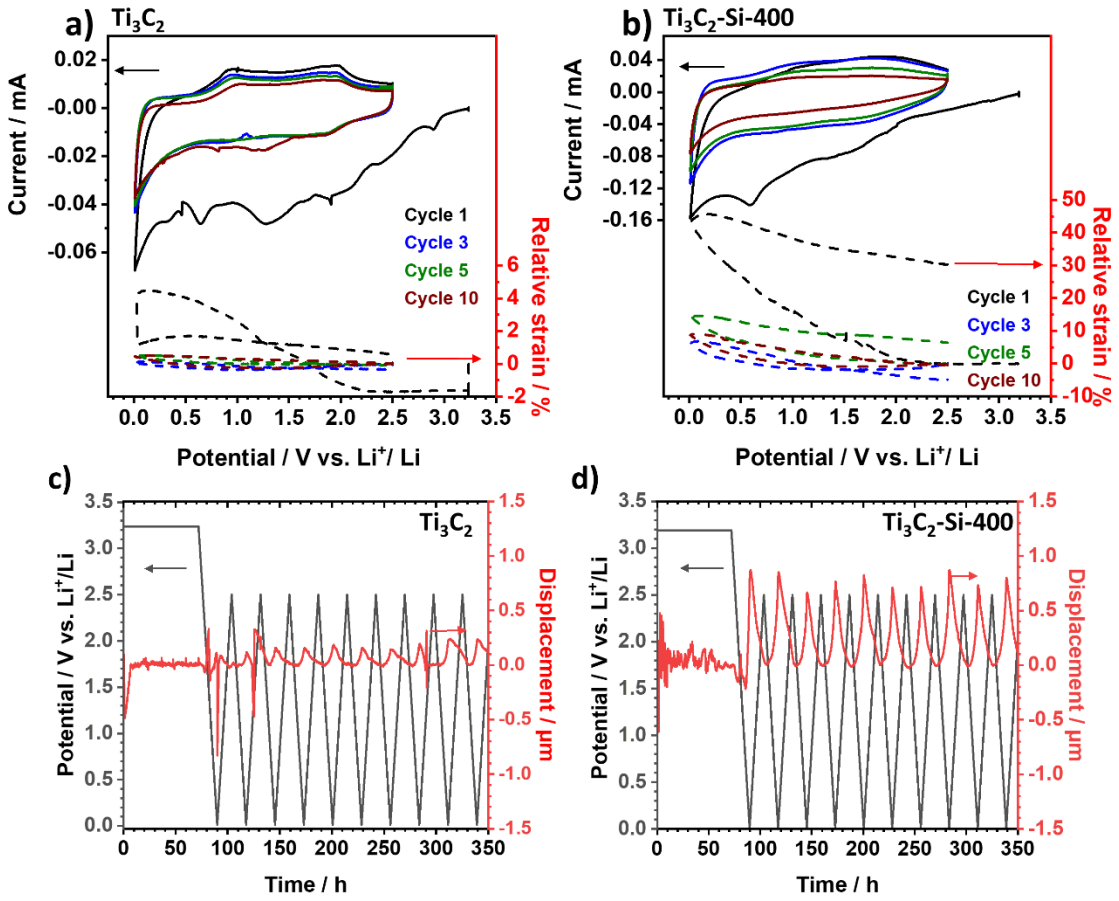

Figure 3. Cyclic voltammograms and corresponding in-situ dilatometric measurements (electrode height change/initial height = strain) from half-cell setup versus Li metal at 0.1 mV s^{-1} in the voltage range 0.01-2.5 V for **a)** non-pillared $Ti_3C_2T_z$ **b)** pillared MXene (Ti_3C_2-Si-400). The electrochemical response of the working electrode (continuous line) can be simultaneously tracked with the height change (dashed line). **c-d)** Potential and relative height change vs. time of MXene electrodes measured by in situ electrochemical dilatometry **c)** for non-pillared $Ti_3C_2T_z$ (electrode thickness of 43 µm) **d)** for pillared MXene (Ti_3C_2-Si-400, electrode thickness of 26 µm). The artifacts which are unrelated to the electrode response had been subtracted as background signals.

Conclusions

In conclusion, silica-pillared $Ti_3C_2T_z$ MXene with an ultralarge interlayer spacing displayed significantly enhanced performance as the negative electrode of a Li-ion battery. In particular, at the high rate of 1 A g^{-1}, the SiO_2-pillared MXene had a capacity over four times that of the non-pillared material (over 150 mAh g^{-1}), and retained over 71% of its initial capacity after

500 cycles. In-situ dilatometry combined with XRD data revealed that the superior cycling performance occurred despite larger volume changes and a decrease in crystallinity, suggesting inhomogeneous interlayer expansion. During lithiation, a constant relative expansion of 3-4% in each cycle is obtained for the pillared MXene sample. In contrast, for the non-pillared MXene, a slightly increasing expansion is obtained with increasing cycle numbers. These results provide key insights for the design of MXene electrodes demonstrating that large interlayer spacings and consistent volume changes, as provided by pillaring techniques, are key for high performance. This is the case even for large (3-4%) expansions, which are well tolerated by pillared MXene.

Acknowledgments

P.A.M. gratefully acknowledges support from the EPSRC Graphene NOWNANO Centre for Doctoral Training. The INM authors thank Eduard Arzt (INM) for his continued support. V.P. acknowledges funding of the MXene-CDI project (PR-1173/11) by the German Research Foundation (DFG, Deutsche Forschungsgemeinschaft). NTR acknowledges the Royal Society (RG170150), Energy Lancaster and Lancaster University for financial support.

References

(1) Naguib, M.; Kurtoglu, M.; Presser, V.; Lu, J.; Niu, J.; Heon, M.; Hultman, L.; Gogotsi, Y.; Barsoum, M. W. Two-Dimensional Nanocrystals Produced by Exfoliation of Ti3 AlC2. *Adv. Mater.* **2011**, *23* (37), 4248–4253. https://doi.org/10.1002/adma.201102306.

(2) Tang, X.; Guo, X.; Wu, W.; Wang, G. 2D Metal Carbides and Nitrides (MXenes) as High-Performance Electrode Materials for Lithium-Based Batteries. *Adv. Energy Mater.* **2018**, *8* (33), 1801897. https://doi.org/10.1002/aenm.201801897.

(3) Anasori, B.; Lukatskaya, M. R.; Gogotsi, Y. 2D Metal Carbides and Nitrides (MXenes) for Energy Storage. *Nat. Rev. Mater.* **2017**, *2* (2), 16098. https://doi.org/10.1038/natrevmats.2016.98.

(4) Naguib, M.; Mochalin, V. N.; Barsoum, M. W.; Gogotsi, Y. 25th Anniversary Article: MXenes: A New Family of Two-Dimensional Materials. *Adv. Mater.* **2014**, *26* (7), 992–1005. https://doi.org/10.1002/adma.201304138.

(5) Greaves, M.; Barg, S.; Bissett, M. A. MXene-Based Anodes for Metal-Ion Batteries. *Batter. Supercaps* **2020**, *3* (3), 214–235. https://doi.org/10.1002/batt.201900165.

(6) Bu, F.; Zagho, M. M.; Ibrahim, Y.; Ma, B.; Elzatahry, A.; Zhao, D. Porous MXenes: Synthesis, Structures, and Applications. *Nano Today*. Elsevier B.V. February 1, 2020, p 100803. https://doi.org/10.1016/j.nantod.2019.100803.

(7) Bao, W.; Tang, X.; Guo, X.; Choi, S.; Wang, C.; Gogotsi, Y.; Wang, G. Porous Cryo-Dried MXene for Efficient Capacitive Deionization. *Joule* **2018**, *2* (4), 778–787. https://doi.org/10.1016/j.joule.2018.02.018.

(8) Zhang, S.; Huang, P.; Wang, J.; Zhuang, Z.; Zhang, Z.; Han, W.-Q. Fast and Universal Solution-Phase Flocculation Strategy for Scalable Synthesis of Various Few-Layered MXene Powders. *J. Phys. Chem. Lett.* **2020**, *11* (4), 1247–1254. https://doi.org/10.1021/ACS.JPCLETT.9B03682.

(9) Kloprogge, J. T. Synthesis of Smectites and Porous Pillared Clay Catalysts: A Review. *J. Porous Mater.* **1998**, *5* (1), 5–41. https://doi.org/10.1023/A:1009625913781.

(10) Luo, J.; Zhang, W.; Yuan, H.; Jin, C.; Zhang, L.; Huang, H.; Liang, C.; Xia, Y.; Zhang, J.; Gan, Y.; Tao, X. Pillared Structure Design of MXene with Ultralarge Interlayer Spacing for High-Performance Lithium-Ion Capacitors. *ACS Nano* **2017**, *11* (3), 2459–2469. https://doi.org/10.1021/acsnano.6b07668.

(11) Luo, J.; Wang, C.; Wang, H.; Hu, X.; Matios, E.; Lu, X.; Zhang, W.; Tao, X.; Li, W. Pillared MXene with Ultralarge Interlayer Spacing as a Stable Matrix for High Performance Sodium Metal Anodes. *Adv. Funct. Mater.* **2019**, *29* (3), 1805946. https://doi.org/10.1002/adfm.201805946.

(12) Luo, J.; Zheng, J.; Nai, J.; Jin, C.; Yuan, H.; Sheng, O.; Liu, Y.; Fang, R.; Zhang, W.; Huang, H.; Gan, Y.; Xia, Y.; Liang, C.; Zhang, J.; Li, W.; Tao, X. Atomic Sulfur Covalently Engineered Interlayers of Ti_3C_2 MXene for Ultra-Fast Sodium-Ion Storage by Enhanced Pseudocapacitance. *Adv. Funct. Mater.* **2019**, *29* (10), 1808107. https://doi.org/10.1002/adfm.201808107.

(13) Tian, W.; VahidMohammadi, A.; Wang, Z.; Ouyang, L.; Beidaghi, M.; Hamedi, M. M.

Layer-by-Layer Self-Assembly of Pillared Two-Dimensional Multilayers. *Nat. Commun.* **2019**, *10* (1), 1–10. https://doi.org/10.1038/s41467-019-10631-0.

(14) Maughan, P. A.; Tapia-Ruiz, N.; Bimbo, N. In-Situ Pillared MXene as a Viable Zinc-Ion Hybrid Capacitor. *Electrochim. Acta* **2020**, *341*, 136061. https://doi.org/10.1016/j.electacta.2020.136061.

(15) Maughan, P. A.; Bouscarrat, L.; Seymour, V.; Shao, S.; Haigh, S. J.; Dawson, R.; Tapia-Ruiz, N.; Bimbo, N. Pillared Mo 2 TiC 2 MXene for High-Power and Long-Life Lithium and Sodium-Ion Batteries . *Nanoscale Adv.* **2021**. https://doi.org/10.1039/d1na00081k.

(16) Zhang, S.; Ying, H.; Yuan, B.; Hu, R.; Han, W.-Q. Partial Atomic Tin Nanocomplex Pillared Few-Layered Ti 3 C 2 T x MXenes for Superior Lithium-Ion Storage. *Nano-Micro Lett. 2020 121* **2020**, *12* (1), 1–14. https://doi.org/10.1007/S40820-020-0405-7.

(17) Zhang, S.; Han, W.-Q. Recent Advances in MXenes and Their Composites in Lithium/Sodium Batteries from the Viewpoints of Components and Interlayer Engineering. *Phys. Chem. Chem. Phys.* **2020**, *22* (29), 16482–16526. https://doi.org/10.1039/D0CP02275F.

(18) Zhang, S.; Ying, H.; Huang, P.; Wang, J.; Zhang, Z.; Yang, T.; Han, W.-Q. Rational Design of Pillared SnS/Ti3C2Tx MXene for Superior Lithium-Ion Storage. *ACS Nano* **2020**, *14* (12), 17665–17674. https://doi.org/10.1021/ACSNANO.0C08770.

(19) Xu, K.; Merlet, C.; Lin, Z.; Shao, H.; Taberna, P. L.; Miao, L.; Jiang, J.; Zhu, J.; Simon, P. Effects of Functional Groups and Anion Size on the Charging Mechanisms in Layered Electrode Materials. *Energy Storage Mater.* **2020**, *33*, 460–469. https://doi.org/10.1016/j.ensm.2020.08.030.

(20) Jäckel, N.; Krüner, B.; Van Aken, K. L.; Alhabeb, M.; Anasori, B.; Kaasik, F.; Gogotsi, Y.; Presser, V. Electrochemical in Situ Tracking of Volumetric Changes in Two-Dimensional Metal Carbides (MXenes) in Ionic Liquids. *ACS Appl. Mater. Interfaces* **2016**, *8* (47), 32089–32093. https://doi.org/10.1021/acsami.6b11744.

(21) Come, J.; Black, J. M.; Lukatskaya, M. R.; Naguib, M.; Beidaghi, M.; Rondinone, A. J.;

Kalinin, S. V.; Wesolowski, D. J.; Gogotsi, Y.; Balke, N. Controlling the Actuation Properties of MXene Paper Electrodes upon Cation Intercalation. *Nano Energy* **2015**, *17*, 27–35. https://doi.org/10.1016/j.nanoen.2015.07.028.

(22) Gao, Q.; Come, J.; Naguib, M.; Jesse, S.; Gogotsi, Y.; Balke, N. Synergetic Effects of K+ and Mg2+ Ion Intercalation on the Electrochemical and Actuation Properties of the Two-Dimensional Ti3C2 MXene. *Faraday Discuss.* **2017**, *199* (0), 393–403. https://doi.org/10.1039/c6fd00251j.

(23) Torkamanzadeh, M.; Torkamanzadeh, M.; Wang, L.; Wang, L.; Zhang, Y.; Zhang, Y.; Budak, Ö.; Budak, Ö.; Srimuk, P.; Presser, V.; Presser, V. MXene/Activated-Carbon Hybrid Capacitive Deionization for Permselective Ion Removal at Low and High Salinity. *ACS Appl. Mater. Interfaces* **2020**, *12* (23), 26013–26025. https://doi.org/10.1021/acsami.0c05975.

(24) Maughan, P. A.; Seymour, V. R.; Bernardo-Gavito, R.; Kelly, D. J.; Shao, S.; Tantisriyanurak, S.; Dawson, R.; Haigh, S. J.; Young, R. J.; Tapia-Ruiz, N.; Bimbo, N. Porous Silica-Pillared MXenes with Controllable Interlayer Distances for Long-Life Na-Ion Batteries. *Langmuir* **2020**, *36* (16), 4370–4382. https://doi.org/10.1021/acs.langmuir.0c00462.

(25) Shuck, C. E.; Sarycheva, A.; Anayee, M.; Levitt, A.; Zhu, Y.; Uzun, S.; Balitskiy, V.; Zahorodna, V.; Gogotsi, O.; Gogotsi, Y. Scalable Synthesis of $Ti_3C_2T_x$ MXene. *Adv. Eng. Mater.* **2020**, *22* (3), 1901241. https://doi.org/10.1002/adem.201901241.

(26) Xie, Y.; Naguib, M.; Mochalin, V. N.; Barsoum, M. W.; Gogotsi, Y.; Yu, X.; Nam, K.-W.; Yang, X.-Q.; Kolesnikov, A. I.; Kent, P. R. C. Role of Surface Structure on Li-Ion Energy Storage Capacity of Two-Dimensional Transition-Metal Carbides. *J. Am. Chem. Soc.* **2014**, *136* (17), 6385–6394. https://doi.org/10.1021/ja501520b.

(27) Wang, Y.; Li, Y.; Qiu, Z.; Wu, X.; Zhou, P.; Zhou, T.; Zhao, J.; Miao, Z.; Zhou, J.; Zhuo, S. Fe3O4@Ti3C2 MXene Hybrids with Ultrahigh Volumetric Capacity as an Anode Material for Lithium-Ion Batteries. *J. Mater. Chem. A* **2018**, *6* (24), 11189–11197. https://doi.org/10.1039/c8ta00122g.

(28) Zhao, N.; Zhang, F.; Zhan, F.; Yi, D.; Yang, Y.; Cui, W.; Wang, X. Fe3+-Stabilized Ti3C2Tx MXene Enables Ultrastable Li-Ion Storage at Low Temperature. *J. Mater. Sci. Technol.* **2021**, *67*, 156–164. https://doi.org/10.1016/j.jmst.2020.06.037.

(29) Augustyn, V.; Come, J.; Lowe, M. A.; Kim, J. W.; Taberna, P.-L.; Tolbert, S. H.; Abruña, H. D.; Simon, P.; Dunn, B. High-Rate Electrochemical Energy Storage through Li+ Intercalation Pseudocapacitance. *Nat. Mater.* **2013**, *12* (6), 518–522. https://doi.org/10.1038/nmat3601.

(30) Wang, J.; Polleux, J.; Lim, J.; Dunn, B. Pseudocapacitive Contributions to Electrochemical Energy Storage in TiO 2 (Anatase) Nanoparticles. *J. Phys. Chem. C* **2007**, *111* (40), 14925–14931. https://doi.org/10.1021/jp074464w.

(31) Chao, H.; Qin, H.; Zhang, M.; Huang, Y.; Cao, L.; Guo, H.; Wang, K.; Teng, X.; Cheng, J.; Lu, Y.; Hu, H.; Wu, M. Boosting the Pseudocapacitive and High Mass-Loaded Lithium/Sodium Storage through Bonding Polyoxometalate Nanoparticles on MXene Nanosheets. *Adv. Funct. Mater.* **2021**, *31* (16), 2007636. https://doi.org/10.1002/adfm.202007636.

(32) Wan, L.; Chua, D. H. C.; Sun, H.; Chen, L.; Wang, K.; Lu, T.; Pan, L. Construction of Two-Dimensional Bimetal (Fe-Ti) Oxide/Carbon/MXene Architecture from Titanium Carbide MXene for Ultrahigh-Rate Lithium-Ion Storage. *J. Colloid Interface Sci.* **2021**, *588*, 147–156. https://doi.org/10.1016/j.jcis.2020.12.071.

(33) Luo, J.; Fang, C.; Jin, C.; Yuan, H.; Sheng, O.; Fang, R.; Zhang, W.; Huang, H.; Gan, Y.; Xia, Y.; Liang, C.; Zhang, J.; Li, W.; Tao, X. Tunable Pseudocapacitance Storage of MXene by Cation Pillaring for High Performance Sodium-Ion Capacitors. *J. Mater. Chem. A* **2018**, *6* (17), 7794–7806. https://doi.org/10.1039/C8TA02068J.

(34) Hahn, M.; Barbieri, O.; Gallay, R.; Kötz, R. A Dilatometric Study of the Voltage Limitation of Carbonaceous Electrodes in Aprotic EDLC Type Electrolytes by Charge-Induced Strain. *Carbon N. Y.* **2006**, *44* (12), 2523–2533. https://doi.org/10.1016/j.carbon.2006.05.002.

(35) Cheng, R.; Hu, T.; Zhang, H.; Wang, C.; Hu, M.; Yang, J.; Cui, C.; Guang, T.; Li, C.; Shi, C.;

Hou, P.; Wang, X. Understanding the Lithium Storage Mechanism of Ti3C2Tx MXene. *J. Phys. Chem. C* **2019**, *123* (2), 1099–1109. https://doi.org/10.1021/acs.jpcc.8b10790.

(36) Tang, X.; Guo, X.; Wu, W.; Wang, G. 2D Metal Carbides and Nitrides (MXenes) as High-Performance Electrode Materials for Lithium-Based Batteries. *Adv. Energy Mater.* **2018**, *8* (33), 1801897. https://doi.org/10.1002/aenm.201801897.

(37) Sun, D.; Wang, M.; Li, Z.; Fan, G.; Fan, L. Z.; Zhou, A. Two-Dimensional Ti3C2 as Anode Material for Li-Ion Batteries. *Electrochem. commun.* **2014**, *47*, 80–83. https://doi.org/10.1016/j.elecom.2014.07.026.

(38) Gnanamuthu, R.; Lee, C. W. Electrochemical Properties of Super P Carbon Black as an Anode Active Material for Lithium-Ion Batteries. *Mater. Chem. Phys.* **2011**, *130* (3), 831–834. https://doi.org/10.1016/j.matchemphys.2011.08.060.

(39) Come, J.; Naguib, M.; Rozier, P.; Barsoum, M. W.; Gogotsi, Y.; Taberna, P.-L.; Morcrette, M.; Simon, P. A Non-Aqueous Asymmetric Cell with a Ti2C-Based Two-Dimensional Negative Electrode. *J. Electrochem. Soc.* **2012**, *159* (8), A1368–A1373. https://doi.org/10.1149/2.003208jes.

(40) Budak; Geißler, M.; Becker, D.; Kruth, A.; Quade, A.; Haberkorn, R.; Kickelbick, G.; Etzold, B. J. M.; Presser, V. Carbide-Derived Niobium Pentoxide with Enhanced Charge Storage Capacity for Use as a Lithium-Ion Battery Electrode. *ACS Appl. Energy Mater.* **2020**, *3* (5), 4275–4285. https://doi.org/10.1021/acsaem.9b02549.

Supporting Information

In-situ Investigation of Expansion during Lithiation of Pillared MXene with Ultralarge Interlayer Distance

Philip A. Maughan,[1] Stefanie Arnold,[2,3] Yuan Zhang,[2,3] Volker Presser,[2,3,4] Nuria Tapia-Ruiz,[5] and Nuno Bimbo[1,6*]

[1] Department of Engineering, Lancaster University, Lancaster, LA1 4YW, United Kingdom
[2] INM - Leibniz Institute for New Materials, Saarbrücken, 66123, Germany
[3] Department of Materials Science and Engineering, Saarland University, 66123 Saarbrücken, Germany
[4] Saarene Saarland Center for Energy Materials and Sustainability, Campus D4.2, 66123 Saarbrücken, Germany
[5] Department of Chemistry, Lancaster University, Lancaster, LA1 4YB, United Kingdom
[6] School of Chemistry, Highfield Campus, University of Southampton, Southampton, SO17 1BJ, United Kingdom

[*] Corresponding author's email: N.Bimbo@soton.ac.uk

Table of Contents

Experimental methods

Materials

The following materials were used without any further purification: Ti_3AlC_2 (Carbon Ukraine Ltd), hydrochloric acid (37.5 mass%, Sigma Aldrich), tetraethylortho silicate (TEOS, 98% purity, Alfa Aesar), 1-dodecylamine (DDA, 97% purity, Alfa Aesar), N-Methyl-2-pyrrolidone (NMP, 99.5% purity, Alfa Aesar), PVDF (99.0% purity, Alfa Aesar), Super P carbon black (99% purity, Alfa Aesar), $LiPF_6$ in diethyl carbonate (DEC) and ethylene carbonate (EC) (1:1 by mass, 99% purity Gotion), copper foil (Tob New Energy).

Synthesis of $Ti_3C_2T_z$

To obtain the MXenes, 3 g of Ti_3AlC_2 were sieved through a -400 mesh sieve (pore size of 38 µm) and added over 10 min to a 6 M HCl solution with pre-dissolved LiF (7.5:1 F to Al ratio). This mixture was heated to 40 °C and left to etch for 48 h with magnetic stirring. The powder was re-dispersed in a 1 M HCl solution for 3 h at room temperature to remove any remaining impurities and to increase the number of -OH surface groups on the MXene.

Pillaring of $Ti_3C_2T_z$ samples

For the pillaring experiments, we applied our previously reported amine-assisted silica pillaring method.[1] Briefly, 0.5 g of the as-made $Ti_3C_2T_z$ MXene were added to a solution of dodecylamine (DDA) dissolved in TEOS in a MXene:DDA:TEOS molar ratio of 1:10:20 under argon. This was stirred in a sealed glass vial under argon at room temperature for 4 h. The black powder was then recovered by vacuum filtration, dried on filter paper under vacuum before being re-dispersed in de-ionized water (25 mL) overnight at room temperature (18 h). The intercalated product was then recovered by vacuum filtration and dried overnight at 60 °C. These samples were then calcined at 400 °C for 5 h under argon with a heating rate of 5 °C min^{-1}.

Characterization

The samples were characterized by X-ray diffraction (XRD) in a Smartlab diffractometer (Rigaku) using Cu-Kα radiation operating in reflection mode with Bragg-Brentano geometry to investigate the crystal structure. Prior to the XRD characterisation, all samples were dried in an oven at 80 °C for 18 h. The black powders were then ground and placed on a silica sample holder and pressed flat with a glass slide.

Scanning electron microscopy (SEM) was carried out in a JEOL JSM-7800F (JEOL), and energy-dispersive x-ray spectroscopy (EDX) was done in a X-Max50 (Oxford Instruments) using an accelerating voltage of 10 kV and a working distance of 10 mm, which were used to study the morphology and elemental composition. For the SEM and SEM-EDS studies, the dried powder samples were dry cast onto a carbon tape support, which was placed on to a copper stub for analysis. To minimize errors from the use of EDS for the estimation of the Si content, large flat particle surfaces were chosen for the EDS mapping.

Electrochemical characterization

To test the pillaring process's effect on the electrochemical performance, the pillared and un-pillared materials were tested in CR2032 coin cells with a half-cell configuration using lithium metal disks as the counter electrode and 1 M $LiPF_6$ in EC/DEC (1:1 mass ratio) as the electrolyte. The MXene was mixed with carbon black (Super P) as a conductive additive and PVDF as the binder in a 75:15:10 mass ratio, respectively. These were added to a few mL of NMP to make a slurry, which was then cast onto a Cu foil current collector, from which electrodes with a diameter of 16 mm were punched. The active mass weighting was around 3 mg cm^{-2}. Coin cells were constructed in an argon-filled glovebox (O_2 and H_2O levels < 0.1 ppm) using Whatman microglass fibre paper as the separator. The charge-discharge tests were carried out on a Neware battery cycler (Neware Battery Technologies Ltd.) at a current density of 20 mA g^{-1} in the voltage range of 0.01-3.0 V vs. Li^+/Li for 100 cycles. For rate capability tests, the cells were cycled at a specific current of 20 mA g^{-1} for one cycle to stabilise the cell followed by five cycles at each rate of 20, 50, 200, 500, 1000 mA g^{-1} before returning to 20 mA g^{-1}. Cyclic voltammetry (CV) measurements were conducted using an Ivium potentiostat (Ivium Technologies BV) with a scan rate of 0.2 mV s^{-1} for five cycles, followed by further cycles at 0.5, 2, 5 mV s^{-1} sweep rates in the voltage range of 0.01-3.0 V vs. Li^+/Li. The

final scan at each rate was used for the calculation of the *b*-values. The relationship between the current (*i*) and scan rate (*v*) is given by Equation (1):

$$i = av^b \quad \textbf{(1)}$$

where *a* and *b* are fitting parameters.[2] A *b*-value of 0.5 corresponds to an ideal diffusion-limited (battery-like) charge storage process whereas a *b*-value of 1 indicates a perfect surface-limited (capacitive-like) process. To calculate the total contribution of capacitive-like processes to the charge storage, deconvolution of the total current into surface capacitive and diffusion controlled intercalation processes was carried out using the method described by Dunn et al, using the Equation (2-3).[3]

$$i(V, v) = k_1(V) + k_2(V)v^{1/2} \quad \textbf{(2)}$$

$$i(V,v)/v^{1/2} = k_1(V)v^{1/2} + k_2(V) \quad \textbf{(3)}$$

Here k_1 and k_2 are potential dependant constants, *i* is the current and is the *v* scan rate. The values for k_1 and k_2 were obtained using Equation (3) by plotting *i* against $v^{1/2}$ for each potential, where a linear fit has k_1 as the gradient and k_2 as the intercept. This was used to calculate the non-diffusion limited ($k_1.v$) and diffusion-limited ($k_2.v^{1/2}$) contributions at each potential for each scan rate studied. The non-diffusion limited contribution to the total charge is typically assumed to represent the capacitive charge. The total capacitive contribution to the charge storage for each scan rate was then calculated by integrating the area of a cyclic voltammogram for the total experimental current and the calculated capacitive current.

In-situ dilatometry

The in-situ dilatometry measurements (height change (strain) of the MXene electrodes during charging and discharging) were conducted by using an ECD-3-nano cell device from EL-CELL (setup adopting the design by Hahn et al.).[4] All cell parts were dried overnight at +80 °C and introduced into an argon-filled glovebox (MBraun Labmaster 130; O_2 and H_2O < 0.1 ppm). The cells were arranged in a two-electrode configuration for electrochemical measurement. The electrode discs were punched out of the electrode films with a diameter of 10 mm (0.785 cm^2) using a press punch (EL-CELL). Film thicknesses were measured inside the glovebox before cell assembly with a digital micrometer from HELIOS PREISSER. The lithium-ion cells contained an MXene electrode (pillared or non-pillared) as working electrode, followed by a fixed glass-ceramic separator so that only the thickness change of the working electrode was measured.

Circular punches lithium chips with a diameter of 11 mm as both counter and reference electrodes were placed on top of the separator. The investigated electrodes were compressed between the separator and a movable titanium plunger. The electrolyte, 1 M $LiPF_6$ salt in a mixture of ethylene carbonate and dimethyl carbonate (EC: DMC; 1:1 by volume, Sigma Aldrich) was filled by vacuum backfilling (approximately 0.5 mL). All electrochemical measurements were carried out at a climate chamber (Binder) with a constant temperature of +25±1 °C. Cyclic voltammetry (CV) measurements were carried out using a VMP3 multi-channel potentiostat/galvanostat from Bio-Logic.After a resting period and stabilization time of 72 h, cyclic voltammograms were recorded at 0.01 mV s^{-1} at voltages in the range of 0.1-2.5 V vs. Li^+/Li.

Ex-situ X-ray diffraction

For the ex-situ X-ray diffraction measurements, the MXene electrodes were cycled for two CV cycles and stopped in the de-lithiated state at 3.0 V vs. Li^+/Li. Cyclic voltammetry was carried out using a VMP3 multi-channel potentiostat/galvanostat from Bio-Logic. All electrochemical measurements were carried out in a climate chamber (Binder) with a constant temperature of +25±1 °C. All CV measurements were carried out with a scan rate of 0.1 mV s^{-1} in a potential window of 0.01-3.0 V vs. Li^+/Li. The cells were then transferred to an Ar-filled glovebox for disassembly. Prior to the XRD measurements, the electrodes were detached from the remaining parts and rinsed with DMC to remove remains of the salt of electrolyte. X-ray diffraction (XRD) measurements of the cycled electrodes were performed with a D8 Advance diffractometer (Bruker AXS) with a copper X-ray source (Cu-Kα (λ = 1.5406 Å), 40 kV, 40 mA). The samples were examined in the range 2θ, ranging from 3.50 ° to 79.02 ° and in steps of 0.02° 2θ.

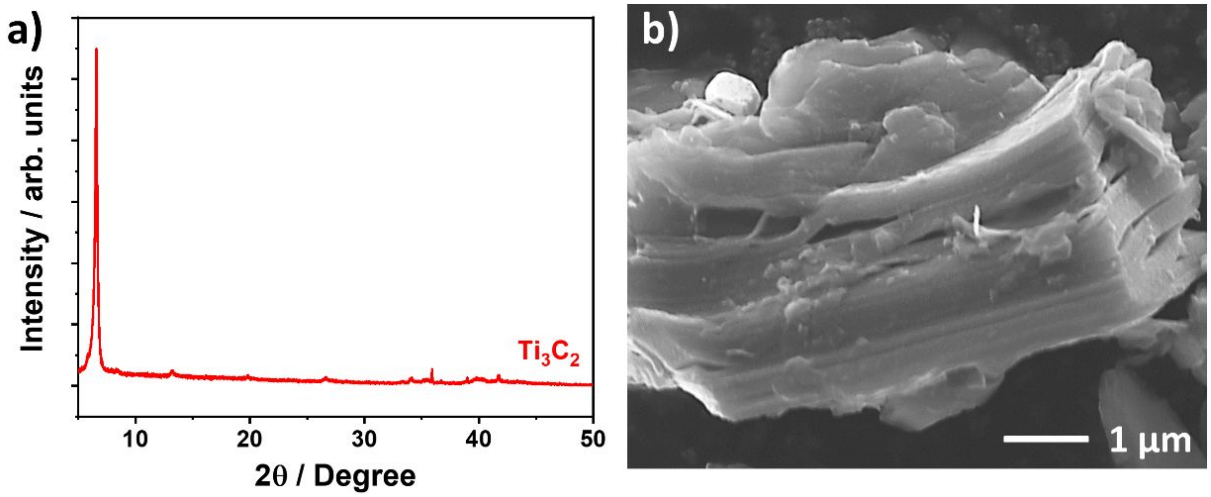

Figure S1. a) X-ray diffractogram of the as-synthesised non-pillared MXene. b) Scanning electron micrograph of the non-pillared MXene.

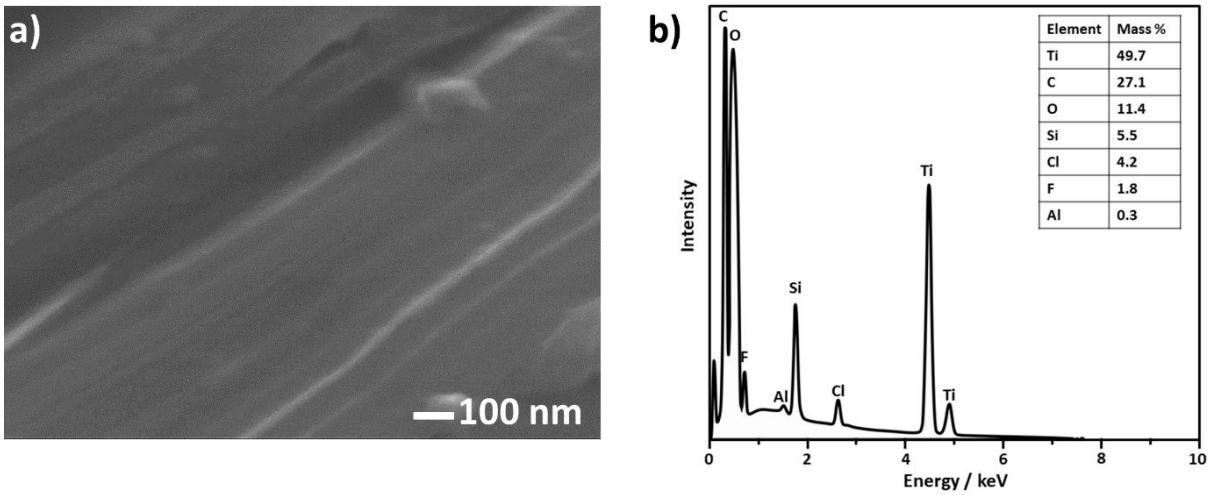

Figure S2. SEM-EDS analysis of the pillared MXene showing that the SiO_2 content is approximately 11 mass% in the pillared material. a) SEM of the analysed region. b) EDS spectrum.

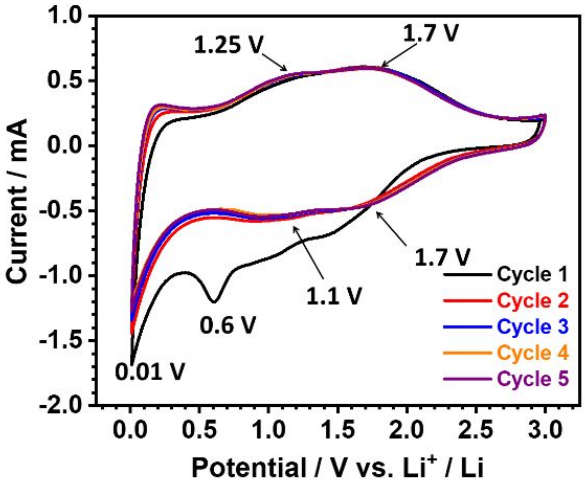

Figure S3. CV data from SiO_2-pillared $Ti_3C_2T_z$. Cells were run in a voltage window of 0.01-3 V vs. Li^+/Li using 1 M $LiPF_6$ in EC:DEC (1:1 mass ratio) as the electrolyte. First five cycles at a scan rate of 0.2 mV s^{-1}. The numbers and arrows highlight reaction peaks.

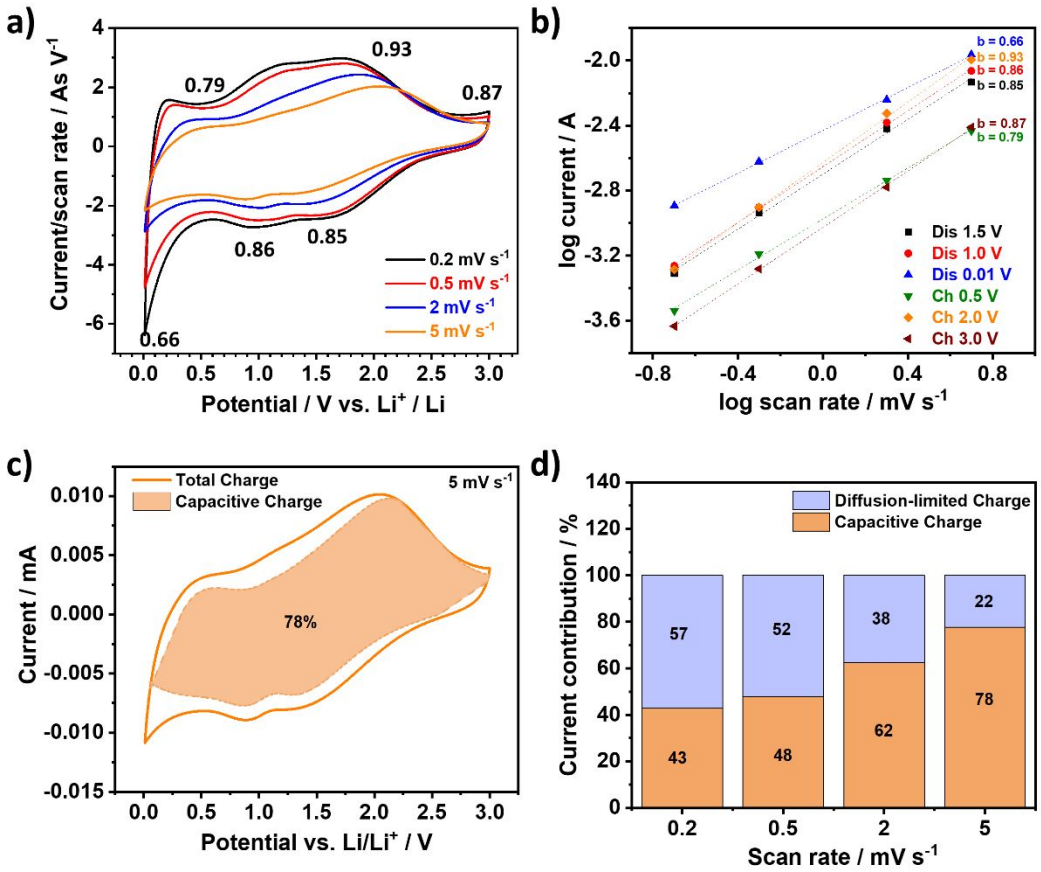

Figure S4. Capacitive contribution to charge storage from CV data for SiO_2-pillared $Ti_3C_2T_z$. Cells were run in a voltage window of 0.01-3 V vs. Li^+/Li using 1 M $LiPF_6$ in EC:DEC (1:1 mass ratio) as the electrolyte. **a)** Cyclic voltammograms when cycled at increasing rates of 0.2, 0.5, 2 and 5 mV s^{-1} in a voltage window of 0.01-3 V vs. Li^+/Li. Two cycles were carried out at each rate, with the second cycle being used for analysis. The numbers show *b*-value for the corresponding peak. **b)** Log current vs. log scan rate plots used to calculate each *b*-value shown in **a)**. R^2 values were greater than 0.999 in all cases, indicating a good fit. **c)** Cyclic voltammogram collected at a scan rate of 5 mV s^{-1} (10 min per sweep), with the capacitive contribution to the current shown by the dashed filled area. The total capacitive contribution to the charge storage at this rate was 78%, as shown by the label in the centre of the plot. **d)** Contribution of both diffusion-limited and capacitive current to the total charge storage at each scan rate: 0.2, 0.5, 2 and 5 mV s^{-1}.

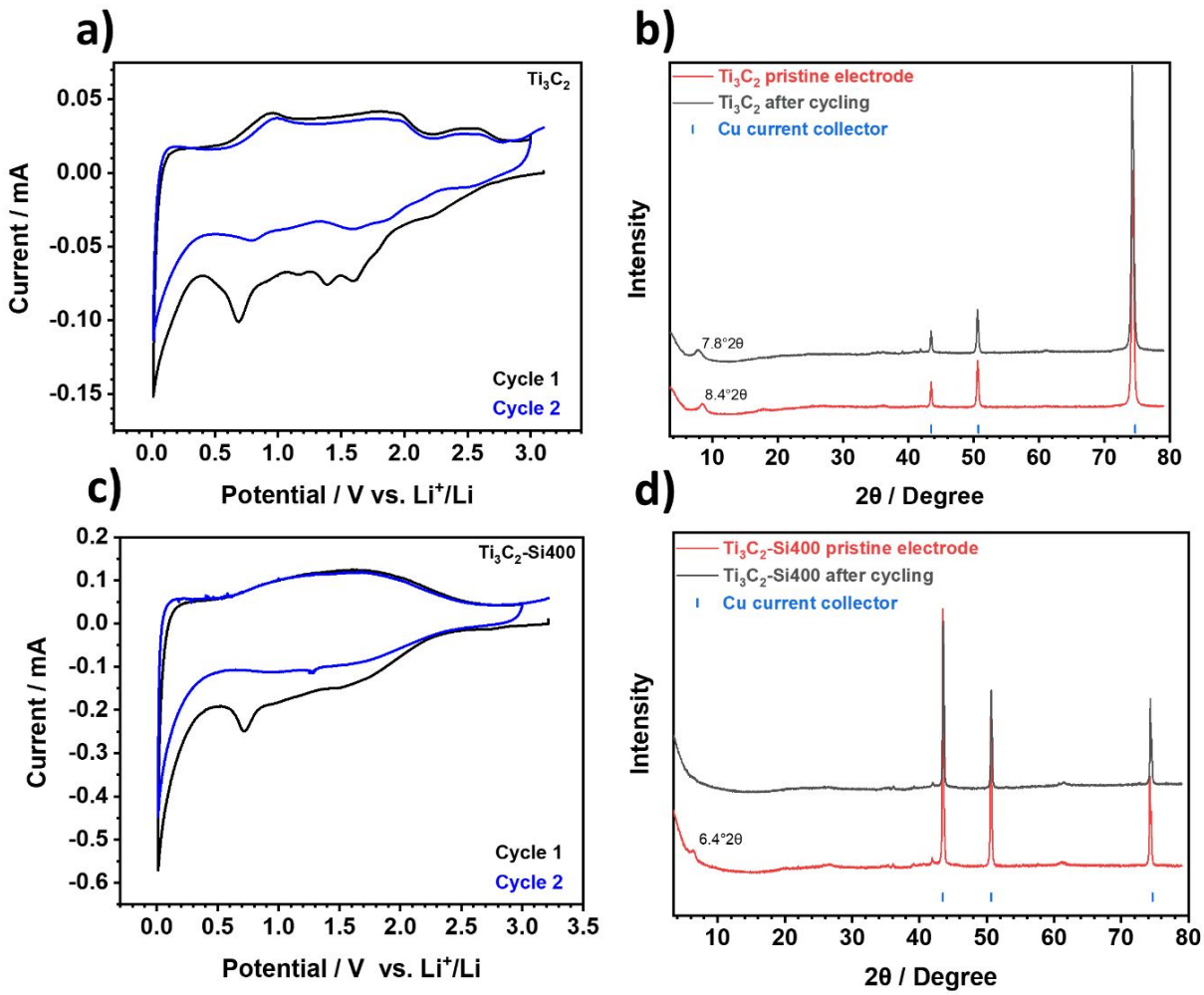

Figure S5. Cyclic voltammograms from half-cell setup at a scan rate of 0.1 mV s^{-1} in the voltage range from 0.01-3 V vs. Li^+/Li using 1 M $LiPF_6$ in EC:ED (1:1 mass ratio) as the electrolyte and corresponding post mortem XRD diffractograms. **a)** First and second cycle of cyclic voltammogram in PEEK cell for non-pillared $Ti_3C_2T_z$ **b)** Correlated post-mortem XRD measurements of cycled non-pillared $Ti_3C_2T_z$ electrode in comparison with the pristine electrode (both coated on copper foil) **c)** First and second cycle of cyclic voltammogram in PEEK cell for pillared MXene (Ti_3C_2-Si-400) **d)** Correlated post-mortem XRD measurements of cycled pillared MXene (Ti_3C_2-Si-400) electrode in comparison with the pristine electrode (both coated on copper foil).

References for the Supporting Information

1. Maughan, P. A. *et al.* Porous Silica-Pillared MXenes with Controllable Interlayer Distances for Long-Life Na-Ion Batteries. *Langmuir* **36**, 4370–4382 (2020).
2. Augustyn, V. *et al.* High-rate electrochemical energy storage through Li^+ intercalation pseudocapacitance. *Nat. Mater.* **12**, 518–522 (2013).
3. Wang, J., Polleux, J., Lim, J. & Dunn, B. Pseudocapacitive contributions to electrochemical energy storage in TiO_2 (anatase) nanoparticles. *J. Phys. Chem. C* **111**, 14925–14931 (2007).
4. Hahn, M., Barbieri, O., Gallay, R. & Kötz, R. A dilatometric study of the voltage limitation of carbonaceous electrodes in aprotic EDLC type electrolytes by charge-induced strain. *Carbon* **44**, 2523–2533 (2006).